JOC The Journal of Organic Chemistry

pubs.acs.org/joc Article

A Promising Nonfullerene Acceptor Containing Boron−Oxygen Heterocycle

Published as part of The Journal of Organic Chemistry special issue "Celebrating Nankai University's Legacy of Excellence in Organic Chemistry".

Yuhong Long,[§] Qiaorong Liu,[§] Shuhui Ding, Tainan Duan, Zhaoyang Yao,* Xiangjian Wan, and Yongsheng Chen*

Cite This: J. Org. Chem. 2025, 90, 16017−16024 Read Online

ACCESS | Metrics & More | Article Recommendations | Supporting Information

ABSTRACT: Exploring nonfullerene acceptors (NFAs) with high luminescent structural "genes" is crucial for suppressing the nonradiative recombination in organic solar cells (OSCs). Herein, a boron−oxygen six-membered heterocycle is first employed to afford two conformationally distinct NFA isomers of CH-S and CH-C. Owing to the electron-lacking nature of boron atoms, both CH-S and CH-C demonstrate a relatively wide bandgap. Interestingly, different ring-fused pathways yield the typical S- and C-shaped molecular conformations, which not only dominate their distinctive intermolecular packing modes but also greatly exert on the fundamental luminescent and optoelectronic properties. Consequently, CH-C-based binary OSCs achieve an excellent efficiency of 11.03%, ranking among the highest values reported for wide-bandgap acceptors with absorption cutoffs below 750 nm. This work first highlights the significant potential of boron−oxygen heterocycles for constructing high-performance wide-bandgap NFAs.

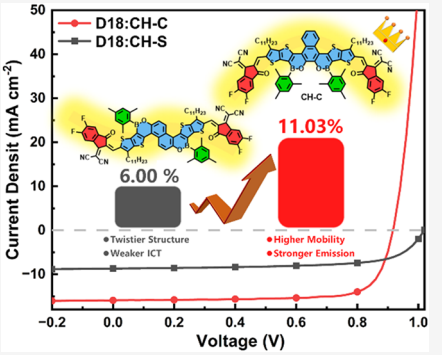

INTRODUCTION

Over recent decades, the advancement of nonfullerene electron acceptors (NFAs) has propelled significant advances in organic solar cells (OSCs),[1−3] with single-junction device efficiencies approaching 21%[4−11] and all-organic tandem solar cells exceeding 20%.[12] Despite these advancements, OSCs continue to exhibit substantially higher energy losses relative to state-of-the-art inorganic perovskite solar cells.[13,14] One of the main sources stems largely from the intrinsically lower dielectric constants of most organic semiconductors and disordered molecular packings, which result in the tightly bound Frenkel excitons upon photoexcitation and sufficient charge recombination sites.[2] Specifically, the particularly critical nonradiative energy loss ($E_{nr,loss}$) is chiefly governed by the photoluminescence quantum yield (PLQY) in narrow-bandgap materials, such as NFAs.[15] Strategies to enhance PLQY include incorporating intrinsically highly emissive moieties[16] or sterically demanding groups[17,18] into the donor/acceptor materials. In addition, the high charge carrier mobility is also an essential performance parameter for organic semiconductors.[19−21] Paradoxically, the molecular structural requirements for high mobility often conflict with those for high luminescence, making the integration of both properties a significant challenge for OSC materials.[22]

It is also worth noting that the advancement of all-organic tandem solar cells lags behind that of single-junction devices. Tandem OSCs, crucial for achieving higher efficiencies, comprise a front subcell and a rear subcell.[23] According to our group's semiempirical theoretical model, the wide-bandgap front subcell should primarily absorb photons in the range of 300−700 nm, possess a large open-circuit voltage (or small energy loss), exhibit excellent charge transfer/transport dynamics, etc.[24] The current wide-bandgap acceptors remain significantly distant from the ideal state. Consequently, the exploration of novel-structure, high-performance wide-bandgap acceptors is imperative to break the critical bottleneck hindering tandem OSC development.

The advancement of blue-emitting materials for organic light-emitting diodes (OLEDs) has matured considerably, which highlights the potential of numerous OLED materials as promising candidates for wide-bandgap, highly luminescent applications.[25,26] Among these, thermally activated delayed fluorescence (TADF) materials are particularly noteworthy. Characterized by spatially separated frontier molecular orbitals (FMOs), TADF materials facilitate small singlet−triplet energy

Received: July 16, 2025
Revised: September 29, 2025
Accepted: October 27, 2025
Published: October 31, 2025

https://doi.org/10.1021/acs.joc.5c01738
J. Org. Chem. 2025, 90, 16017−16024

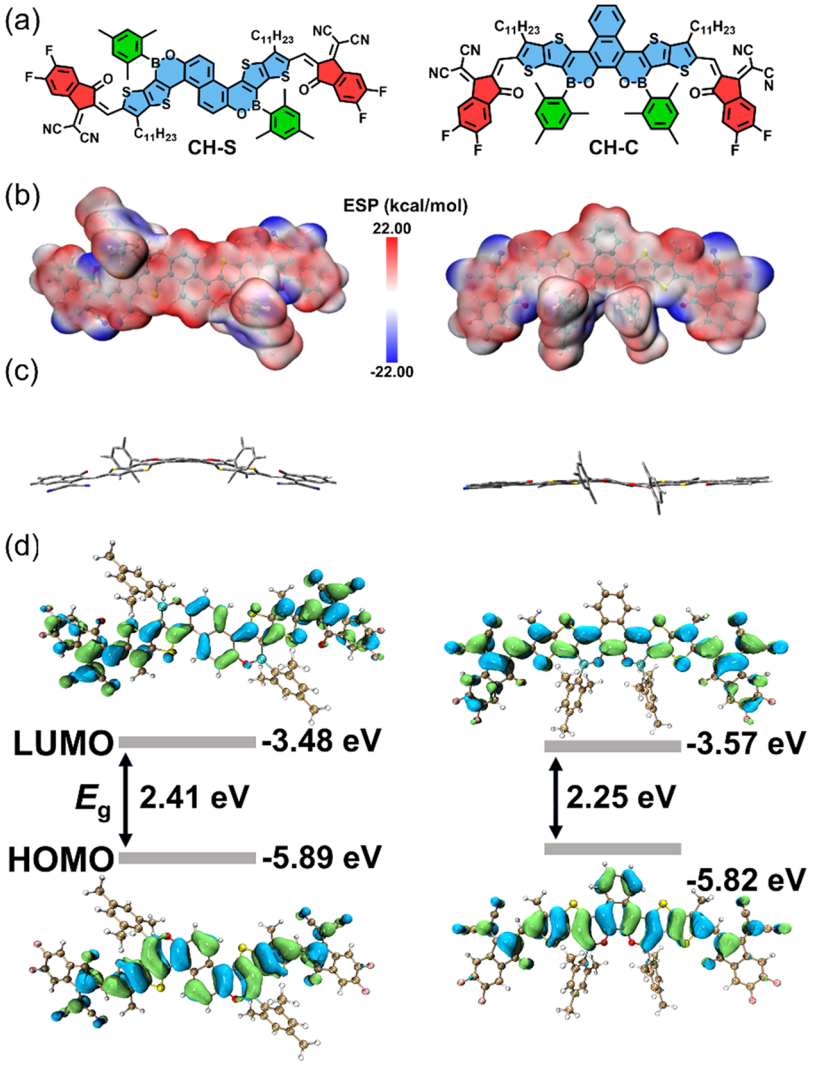

Figure 1. (a) Chemical structures of CH-S and CH-C. (b) Calculated ESP. (c) Side view of optimized molecular geometries. (d) Calculated HOMO and LUMO energy levels and molecular frontier orbital distributions. The ESP and molecular orbitals were analyzed using Multiwfn.[34,35] The values of the isodensity surface were fixed at 0.02.

gaps (ΔE_{ST}), thereby enabling efficient harvesting of triplet excitons.[27] Especially, multiresonance TADF (MR-TADF) materials, exemplified by B−N structures pioneered by Hatakeyama et al., achieve alternating localization of FMOs through electron-donating atoms positioned para or ortho to boron-based electron-accepting units, further minimizing ΔE_{ST} on the premise of keeping a relatively planar molecular conformation.[28] Building on this concept, Liu et al. developed the wide-bandgap NFA BNTT2F by incorporating a B−N covalent bond into an electron acceptor, achieving a power conversion efficiency (PCE) of 8.3%.[29]

Recently, She et al. have extensively explored a series of B−O fused heterocycles, which exhibit low aromaticity, weak electron-accepting nature, intrinsically high luminescence, excellent thermal and chemical stability, etc.[30,31] Therefore, we envisioned that the B−O structural motif holds significant promise for application in wide-bandgap acceptor materials. To enable conjugation extension and provide a sufficient aromatic surface for the desired FMO separation around the boron−oxygen heterocycle, naphthalene was chosen as the central ring. Furthermore, inspired by the molecular conformations of prevalent acceptor materials like Y6[32] and ITIC,[33] we also sought to investigate the impact of C-shaped versus S-shaped molecular geometries in B−O fused heterocycle-based acceptors. Consequently, the B−O six-membered heterocycles were constructed by fusing to the different positions of the central naphthalene, leading to the S-shaped NFA of CH-S and C-shaped NFA of CH-C, as depicted in Figure 1a. The mesityl group serves dually as a protecting group for the boron atom and as a steric unit to modulate luminescence and charge transport. A comprehensive suite of studies, including density functional theory (DFT) calculations, single-crystal analysis, and nanomorphology characterization, has been conducted to elucidate the influence of B−O heterocycle and molecular conformation (S vs C) on intrinsic optoelectronic properties of two NFAs. Ultimately, the binary OSC utilizing CH-C delivered an outstanding PCE of 11.03%. This PCE ranks among the highest values reported for wide-bandgap acceptors exhibiting absorption cutoffs below 750 nm. Our study demonstrates the promise of novel organic boron−oxygen structures for high-performance wide-bandgap NFAs, while elucidating the significant impact of molecular conformation on optoelectronic properties.

https://doi.org/10.1021/acs.joc.5c01738
J. Org. Chem. 2025, 90, 16017−16024

Scheme 1. Synthesized Routes to CH-S and CH-C

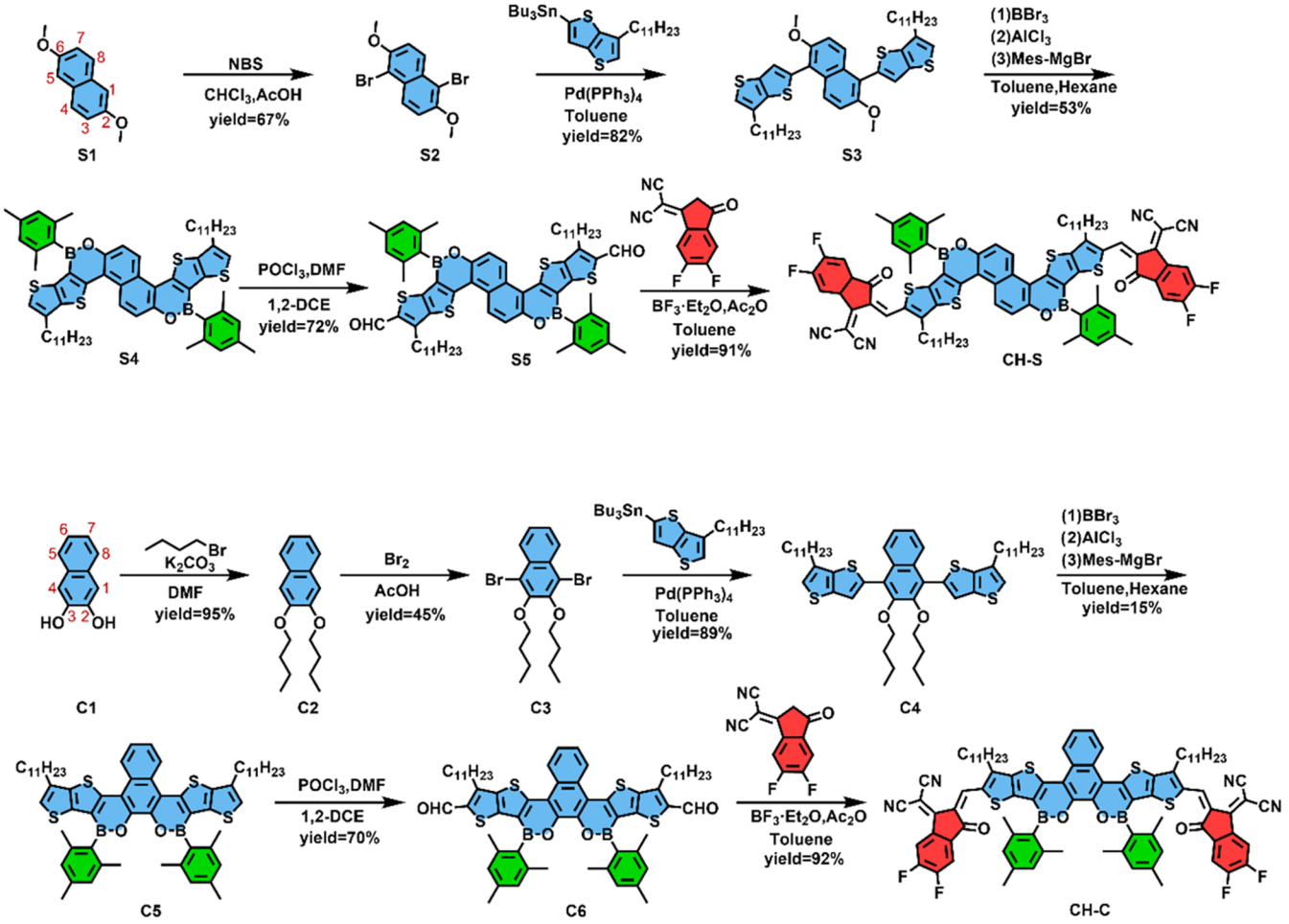

RESULTS AND DISCUSSION

As shown in Figure 1b,c, both NFAs adopt predominantly planar structures overall. Among them, CH-S exhibits a more twisted conformation, while CH-C possesses superior planarity that is expected to enhance intermolecular $\pi-\pi$ interactions. The electrostatic potential (ESP) maps reveal that regions of high electron density are concentrated mainly on the terminal acceptor units for both molecules with relatively higher density also observed on the mesityl groups. This latter effect, which is different from that of Y6 that employs an electron-rich pyrrole ring, may arise because the phenyl ring directly attached to boron draws electron density from the three methyl groups into the π-system of the aromatic ring. Figure 1d presents the FMO energy levels and spatial distributions. Both molecules display highest occupied molecular orbitals (HOMOs) primarily localized on the central region and lowest unoccupied molecular orbitals (LUMOs) concentrated on the terminal units, aligning with the characteristic A-D-A-type acceptor architecture.[36] Notably, the obvious differences in HOMO distribution on the central naphthalene ring could be observed. This is probably attributed to the different bridging ways on the naphthalene unit, which partially disrupts orbital delocalization along its long axis. Therefore, naphthalene unit shows more electron-donating properties for the boron−oxygen heterocycle fused at the ortho-position (oxygen linkage), further leading to an enhanced intramolecular charge transfer (ICT) and a narrower bandgap for CH-C. The direction and magnitude of molecular dipole moments are also illustrated in Figure S1. The S-shaped CH-S, characterized by a center of symmetry, displays a dipole moment oriented perpendicular to the molecular plane. In contrast, the C-shaped CH-C, exhibiting axial symmetry, possesses an in-plane dipole moment directed perpendicular to its long molecular axis, extending from the central electron-donating naphthalene core to the electron-deficient terminal groups. The significant differences in dipole moment characteristics are also anticipated to substantially influence their optoelectronic properties.[37] Additional detailed calculation results can be found in Tables S21−S23.

We initially synthesized the boron−oxygen six-membered heterocycle fused at the 2,6-positions of naphthalene, yielding the target compound S4 with high efficiency (Scheme 1). However, attempts to prepare the 2,3-position fused isomer via identical protocols proved unsuccessful. We observed this outcome aligns with She's report,[30] where ortho-methoxy-substituted substrates similarly failed to produce the corresponding BO7a and BO7b. Consequently, we analyzed the reaction products by nuclear magnetic resonance (NMR) and Fourier transform ion cyclotron resonance high-resolution mass spectrometry (HRMS), identifying a boron-ester analogue as the primary byproduct (Figures S20, S33, and S34). We hypothesized that the close proximity of the two methoxy groups in the 2,3-dimethoxynaphthalene precursor is responsible: after demethylation of one methoxy group by

https://doi.org/10.1021/acs.joc.5c01738
J. Org. Chem. 2025, 90, 16017−16024

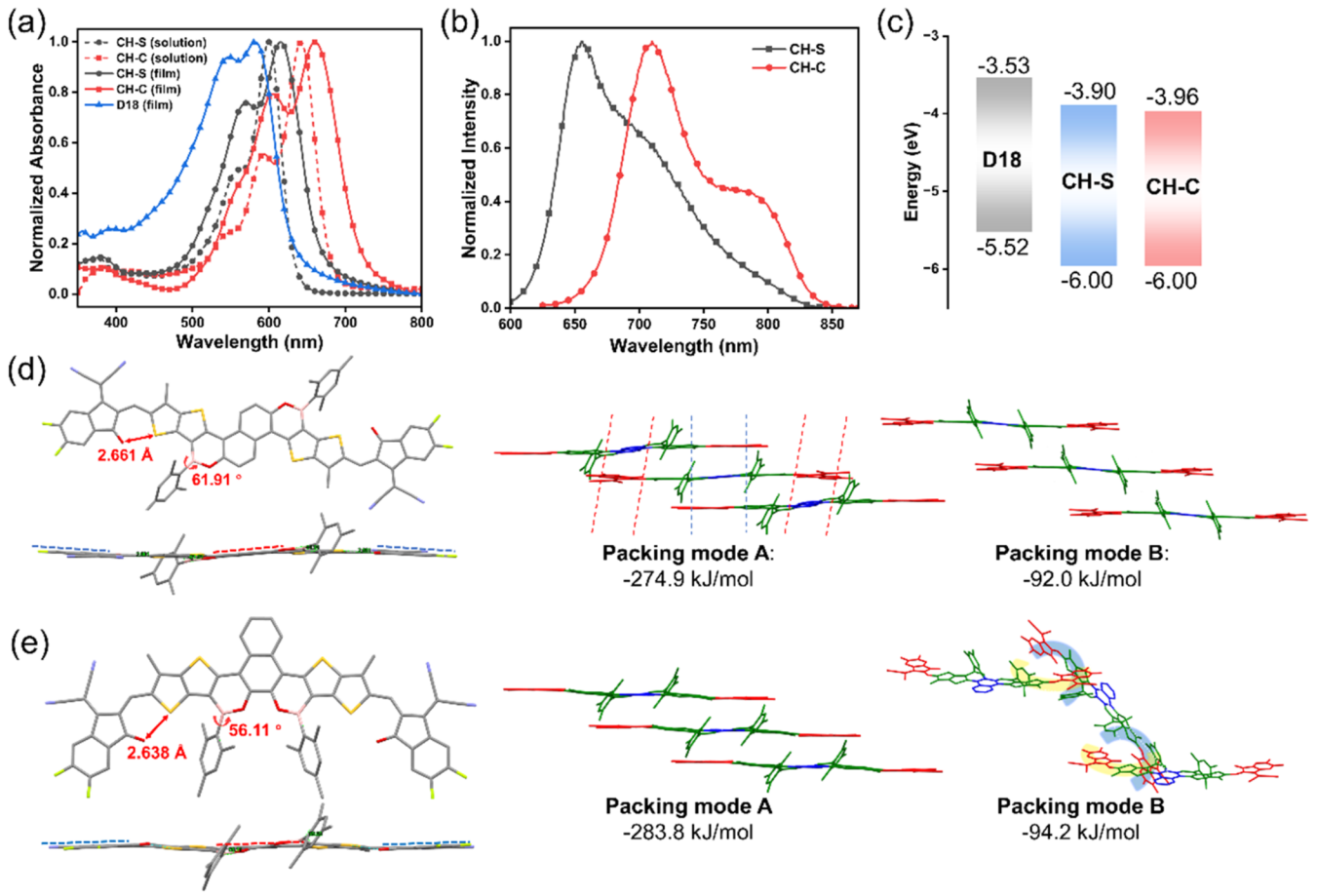

Figure 2. (a) Normalized UV−vis absorption spectra of diluted chloroform solution and neat film for D18, CH-S, and CH-C. (b) Normalized photoluminescence spectra of diluted chloroform solution for CH-S and CH-C. (c) Energy level diagram of D18, CH-S, and CH-C neat film derived from CV. (d, e) Single-crystal structures, main packing mode, and intermolecular potentials of CH-S and CH-C, respectively.

boron tribromide (BBr_3), the generated boron species intramolecularly reacts with the adjacent second methoxy group, preventing its reaction with another equivalent of BBr_3 and leading to boronic ester formation. To redirect the reaction pathway, we explored steric modulation, altered addition sequences, and a controlled reaction temperature. Specifically, methoxy groups were replaced with n-butoxy groups, the addition order was reversed (slow addition of the dimethoxynaphthalene substrate to BBr_3), and the demethylation step was conducted at a lower temperature. These modifications helped to afford the desired compound C5 successfully, albeit in a moderate yield. To the best of our knowledge, this represents the first successful synthesis of ortho-fused boron−oxygen heterocycles via one-pot borylation using ortho-alkoxy substrates. Subsequent formylation of both core intermediates via the Vilsmeier−Haack reaction, followed by Knoevenagel condensation with the terminal acceptor (1,1-dicyanomethylene-3-indanone), ultimately furnished target molecules CH-C and CH-S. Comprehensive characterization included ^1H and ^{13}C NMR spectroscopy for all compounds, with some important intermediates and final NFAs verified by HRMS (Figures S14−S44).

Figure 2a presents the normalized UV−vis absorption spectra for both molecules. CH-S exhibits the solution/film absorption maxima (λ_{max}) at 600:615 nm, while CH-C shows significantly red-shifted λ_{max} values at 641:660 nm, consistent with its narrower calculated bandgap (Figure 1d). CH-C also displays a broader absorption profile and offers better spectral complementarity with the donor polymer D18.[38,39] Normalized photoluminescence (PL) spectra (Figure 2b) reveal that CH-C has a relatively narrower emission peak with a distinct shoulder, whereas CH-S exhibits a broad, featureless emission band. This suggests that CH-S has a higher density of vibrational states, potentially indicative of greater energetic disorder and a higher propensity for nonradiative decay via vibrational relaxation.[40,41] The Stokes shifts of CH-C and CH-S in dilute chloroform solution were determined to be 68 and 55 nm, respectively, calculated from the difference between the maximum absorption peak in the UV−vis spectrum and the maximum emission peak in the PL spectrum. The smaller Stokes shift observed for CH-S suggests a smaller excited-state relaxation energy, which could contribute to reducing the open-circuit voltage loss in related devices.[42] Subsequent PLQY measurements (Figure S2) confirmed the significantly higher PLQY for CH-C, demonstrating its superior luminescent properties compared to CH-S. Electrochemical characterization by cyclic voltammetry (CV) (Figure S3) showed comparable optical bandgaps for both molecules. However, the LUMO energy level of CH-C is lowered by approximately 0.06 eV relative to those of CH-S. This indicates that modifying the fusion mode on the naphthalene ring allows fine-tuning of the energy levels.

Single-crystal X-ray diffraction (XRD) analysis provided detailed insights into the molecular conformation and packing

https://doi.org/10.1021/acs.joc.5c01738
J. Org. Chem. 2025, 90, 16017−16024

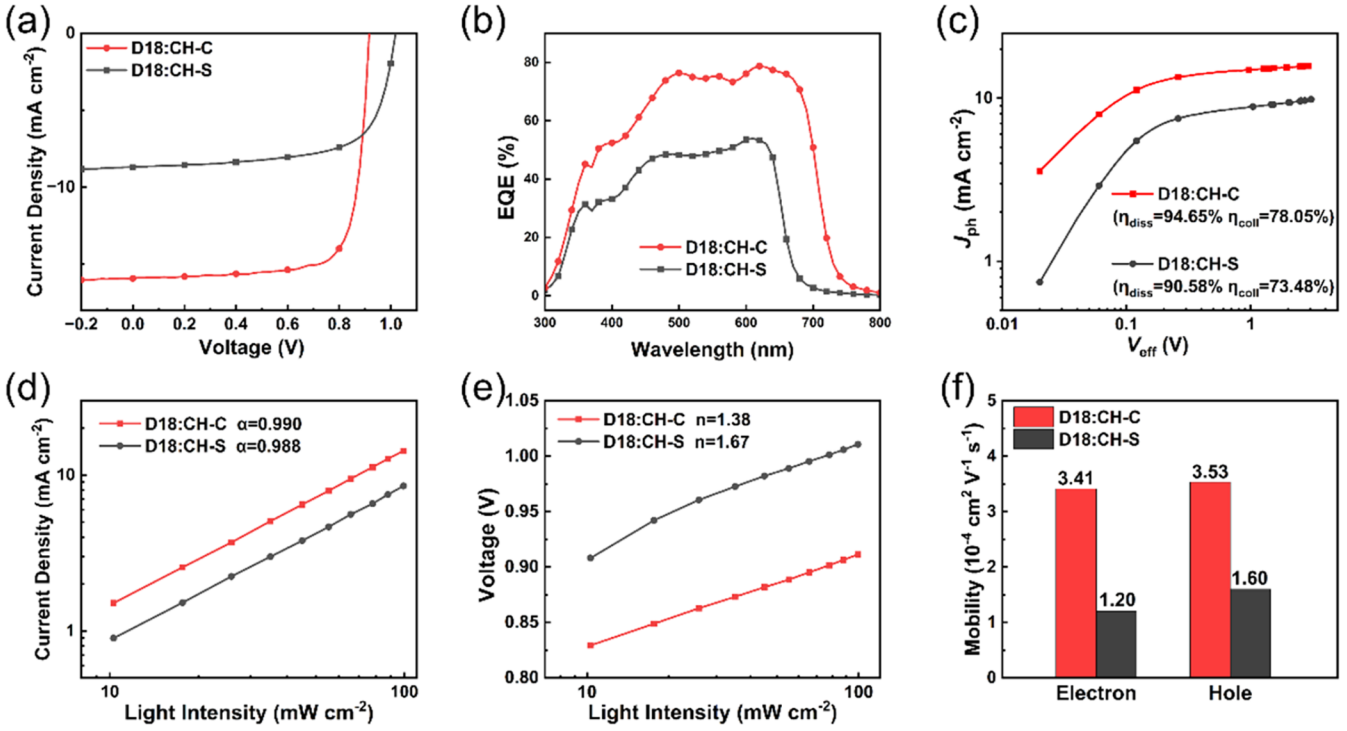

Figure 3. (a) $J-V$ curves, (b) EQE plots, (c) saturation current density (J_{ph}) versus effective voltage (V_{eff}) curves indicating η_{diss} and η_{coll}, (d) J_{sc} versus light intensity curves, (e) V_{oc} versus light intensity curves, and (f) charge mobility of blended films.

Table 1. Summary of Device Parameters for Optimized OSCs[a]

active layer	V_{oc} (V)	J_{sc} (mA cm^{-2})	cal. J_{sc}[b] (mA cm^{-2})	FF (%)	PCE (%)
D18:CH-S	1.019 (0.91 ± 0.007)	8.69 (15.84 ± 0.23)	8.27	67.78 (67.49 ± 1.47)	6.00 (6.01 ± 0.07)
D18:CH-C	0.914 (1.017 ± 0.003)	15.83 (8.76 ± 0.22)	15.11	76.38 (76.31 ± 0.76)	11.03 (10.97 ± 0.22)

[a]The champion and statistical parameters were out/in parentheses, respectively. The statistical ones were derived from 10 devices (Tables S10 and S11). [b]Current densities afforded by EQE plots.

modes of two isomers (Figures 2d,e, S4, and S5). Both molecules adopt relatively planar conformations, although CH-S exhibits a dihedral angle of ∼8.2° between its end groups and central naphthalene. CH-C mainly displays two packing motifs (with intermolecular potentials over 90 kJ/mol). The first one involves stacking of the electron-deficient end group over the electron-donating central core, which is driven primarily by Coulombic interactions characteristic of J-aggregation and beneficial for both charge transport and fluorescence.[22,43] The second motif arises from a "crab-claw" like chelation site formed between the end group and the mesityl group on an adjacent molecule. This sterically driven interaction leads to X-like aggregation, which is potentially less favorable for charge transport than J-aggregation but could still enhance fluorescence.[44] CH-S also exhibits two packing modes. The primary one is similar to CH-C's J-aggregation. However, the dihedral angle between the end-group plane and central naphthalene plane confines molecular alignment to partial parallelism (end-group/core), potentially attenuating overall intermolecular interactions and lowering the interaction energy. This is expected to negatively impact the charge transport in active layers. The secondary packing mode for CH-S involves $\pi-\pi$ interactions between bithiophene units. Steric hindrance from the central core and end groups weakens these interactions and increases intermolecular distances, further compromising the charge transport capability of CH-S. To gain further insight into the charge transport properties of the two molecules, we subsequently performed calculations of the orbital overlap integrals. As shown in Table S1, the results indicate that both packing modes of CH-C exhibit relatively high values for both the HOMO overlap integral (J_{H-H}) and the LUMO overlap integral (J_{L-L}), suggesting that both modes contribute to hole and electron transport. In contrast, packing mode B of CH-S shows negligible contributions to charge transport, which likely accounts for the overall inferior charge transport capability of CH-S compared with CH-C. Subsequently, we carried out charge mobility measurements on the neat films of both molecules, as summarized in Table S2. The results indicate that CH-C exhibits significantly higher electron and hole mobilities than CH-S, which is consistent with the foregoing analysis.

The deep-lying HOMO and LUMO levels of both NFAs motivated the selection of D18 polymer as the donor material in OSC active layers, and the device architecture was ITO/PEDOT:PSS/Active layer/PNDIT-F3N/Ag (detailed device optimization can be found in Tables S3−S15, and the chemical structures of PNDIT-F3N and PEDOT:PSS can be found in Figure S6). Figure 3a and Table 1 present the champion current density−voltage (J-V) characteristics and photovoltaic parameters, respectively. The D18:CH-C binary OSC achieved a maximum PCE of 11.03%, placing it among the highest reported values for wide-bandgap acceptor-based OSCs with absorption cutoffs below 750 nm (Table S16). Although CH-S yielded a higher open-circuit voltage (V_{OC}) of 1.019 V, its

https://doi.org/10.1021/acs.joc.5c01738
J. Org. Chem. 2025, 90, 16017−16024

narrower absorption range and greater spectral overlap with D18 resulted in a lower short-circuit current density (J_{SC}), leading to an inferior PCE compared to CH-C. External quantum efficiency (EQE) spectra (Figure 3b) indicate suppressed EQE values and narrower photoresponse ranges in CH-S-based devices relative to CH-C-based OSCs. One of the reasons should be the more efficient exciton dissociation in CH-C-based device (Figure 3c), consistent with the higher photoluminescence quenching efficiency observed in D18:CH-C blend film (Figure S7) and exciton binding energy from calculation (Table S17). To probe charge recombination mechanisms, light intensity dependence studies of J_{SC} and V_{OC} were conducted (Figure 3d,e). For both measurements, the fitted exponents (α and n, respectively) for CH-C-based devices are closer to unity, signifying weaker bimolecular recombination and more efficient exciton dissociation compared to the CH-S-based device.[45,46] Charge carrier mobility, which could reflect the charge transport capability of materials, was further evaluated (Figure 3f). CH-C-based devices possess not only the higher overall carrier mobility but also more balanced hole-to-electron mobility ratio (1.04 for CH-C and 1.33 for CH-S) compared to the CH-S-based one. This is also helpful for achieving a better fill factor (FF) and J_{SC} for CH-C-based OSCs.

Atomic force microscopy (AFM) images of the blend films (Figure S8) reveal a more pronounced fibrillar network morphology for D18:CH-C blend, thereby enhancing charge carrier mobility. Furthermore, D18:CH-C exhibits relatively larger phase separation domains, attributed to the lower miscibility between CH-C and D18, as corroborated by a higher Flory–Huggins interaction parameter (Figure S9 and Table S18). Two-dimensional grazing-incidence wide-angle X-ray scattering (2D GIWAXS) was used to analyze molecular packing within the blend films (Figure S10 and Table S19). Both blends show a significantly stronger scattering signal at $q \approx 1.80$ Å^{-1}. The XRD patterns derived from the single-crystal data (Figure S11) are roughly consistent with this result, suggesting that the primary molecular packing modes were maintained in the blend film. Additionally, the D18:CH-C blend demonstrates reduced π-π stacking distances (d) and extended crystal coherence lengths (CCL) in both in-plane (IP) and out-of-plane (OOP) orientations, reflecting superior molecular packing density and long-range order that significantly enhance charge transport capabilities in OSCs.

CONCLUSION

The boron–oxygen six-membered heterocycle was applied in NFAs for the first time and rendered two isomeric wind-bandgap NFAs of CH-S and CH-C by strategically varying the fusion positions on the central naphthalene core. The distinct fusion sites on the naphthalene ring not only dominate their distinctive intermolecular packing modes but also greatly exert on the fundamental luminescent and optoelectronic properties of NFAs. The C-shaped CH-C exhibits the enhanced electron-donating capability from the naphthalene unit, strengthens the ICT effect, and facilitates efficient intermolecular π–π interactions. For example, benefiting from the more planar molecular conformation, CH-C adopts a J-aggregation mode with a higher intermolecular potential, contributing to superior photoluminescence and enhanced charge transport properties. Additionally, CH-C's unique "crab-claw" like chelation site enables an X-like aggregation behavior, which further boosts its luminescent properties in the aggregated state. The D18:CH-C binary OSC system achieved a remarkable PCE of 11.03%, representing one of the highest reported values for wide-bandgap binary OSCs exhibiting absorption cutoffs below 750 nm. This study accomplishes two significant advances: (1) it establishes boron–oxygen six-membered heterocycles as highly promising building blocks for wide-bandgap OSC materials and (2) systematically demonstrates how molecular conformation engineering critically governs optoelectronic properties. These findings provide a design roadmap for developing next-generation, high-performance OSC materials based on boron–oxygen heterocyclic architectures.

ASSOCIATED CONTENT

Data Availability Statement

The data underlying this study are available in the published article and its Supporting Information.

Supporting Information

The Supporting Information is available free of charge at https://pubs.acs.org/doi/10.1021/acs.joc.5c01738.

Materials and methods, experimental section, and additional figures and tables (PDF)

Accession Codes

Deposition Numbers 2472282–2472283 contain the supplementary crystallographic data for this paper. These data can be obtained free of charge via the joint Cambridge Crystallographic Data Centre (CCDC) and Fachinformationszentrum Karlsruhe Access Structures service.

AUTHOR INFORMATION

Corresponding Authors

Zhaoyang Yao − *State Key Laboratory of Elemento-Organic Chemistry, Frontiers Science Center for New Organic Matter, The Centre of Nanoscale Science and Technology and Key Laboratory of Functional Polymer Materials, Institute of Polymer Chemistry, College of Chemistry, Renewable Energy Conversion and Storage Center (RECAST), Frontiers Science Center for New Organic Matter, Nankai University, Tianjin 300071, China;* orcid.org/0000-0003-1384-183X; Email: zyao@nankai.edu.cn

Yongsheng Chen − *State Key Laboratory of Elemento-Organic Chemistry, Frontiers Science Center for New Organic Matter, The Centre of Nanoscale Science and Technology and Key Laboratory of Functional Polymer Materials, Institute of Polymer Chemistry, College of Chemistry, Renewable Energy Conversion and Storage Center (RECAST), Frontiers Science Center for New Organic Matter, Nankai University, Tianjin 300071, China;* orcid.org/0000-0003-1448-8177; Email: yschen99@nankai.edu.cn

Authors

Yuhong Long − *State Key Laboratory of Elemento-Organic Chemistry, Frontiers Science Center for New Organic Matter, The Centre of Nanoscale Science and Technology and Key Laboratory of Functional Polymer Materials, Institute of Polymer Chemistry, College of Chemistry, Renewable Energy Conversion and Storage Center (RECAST), Frontiers Science Center for New Organic Matter, Nankai University, Tianjin 300071, China*

Qiaorong Liu − *State Key Laboratory of Elemento-Organic Chemistry, Frontiers Science Center for New Organic Matter, The Centre of Nanoscale Science and Technology and Key Laboratory of Functional Polymer Materials, Institute of*

Polymer Chemistry, College of Chemistry, Renewable Energy Conversion and Storage Center (RECAST), Frontiers Science Center for New Organic Matter, Nankai University, Tianjin 300071, China

Shuhui Ding − *State Key Laboratory of Elemento-Organic Chemistry, Frontiers Science Center for New Organic Matter, The Centre of Nanoscale Science and Technology and Key Laboratory of Functional Polymer Materials, Institute of Polymer Chemistry, College of Chemistry, Renewable Energy Conversion and Storage Center (RECAST), Frontiers Science Center for New Organic Matter, Nankai University, Tianjin 300071, China*

Tainan Duan − *Chongqing Institute of Green and Intelligent Technology, Chinese Academy of Sciences, Chongqing 400714, China;* orcid.org/0000-0002-6010-4501

Xiangjian Wan − *State Key Laboratory of Elemento-Organic Chemistry, Frontiers Science Center for New Organic Matter, The Centre of Nanoscale Science and Technology and Key Laboratory of Functional Polymer Materials, Institute of Polymer Chemistry, College of Chemistry, Renewable Energy Conversion and Storage Center (RECAST), Frontiers Science Center for New Organic Matter, Nankai University, Tianjin 300071, China;* orcid.org/0000-0001-5266-8510

Complete contact information is available at: https://pubs.acs.org/10.1021/acs.joc.5c01738

Author Contributions

[§]Y.L. and Q.L. contributed equally to this work. The synthetic works were carried out by Y.L. The device optimizations and measurements were carried out by Q.L. and S.D. Y.L. performed the DFT calculations. Z.Y., X.W., and Y.C. conceived and directed the study and revised the manuscript. T.D. helped to analyze the data and commented on the manuscript.

Notes

The authors declare no competing financial interest.

■ ACKNOWLEDGMENTS

The authors gratefully acknowledge the financial support from the Ministry of Science and Technology of the People's Republic of China, National Key R&D Program of China (2022YFB4200400), National Natural Science Foundation of China (22361132530, 52025033, 52373189, 22479081, 22309090), and Natural Science Foundation of Tianjin (23JCZDJC01160).

■ REFERENCES

(1) Zhang, G.; Lin, F. R.; Qi, F.; Heumüller, T.; Distler, A.; Egelhaaf, H.-J.; Li, N.; Chow, P. C. Y.; Brabec, C. J.; Jen, A. K. Y.; Yip, H. L. Renewed Prospects for Organic Photovoltaics. *Chem. Rev.* **2022**, *122*, 14180−14274.

(2) Zhang, G.; Zhao, J.; Chow, P. C. Y.; Jiang, K.; Zhang, J.; Zhu, Z.; Zhang, J.; Huang, F.; Yan, H. Nonfullerene Acceptor Molecules for Bulk Heterojunction Organic Solar Cells. *Chem. Rev.* **2018**, *118*, 3447−3507.

(3) Wang, J.; Xie, Y.; Chen, K.; Wu, H.; Hodgkiss, J. M.; Zhan, X. Physical insights into non-fullerene organic photovoltaics. *Nat. Rev. Phys.* **2024**, *6*, 365−381.

(4) Guan, S.; Li, Y.; Xu, C.; Yin, N.; Xu, C.; Wang, C.; Wang, M.; Xu, Y.; Chen, Q.; Wang, D.; et al. Self-Assembled Interlayer Enables High-Performance Organic Photovoltaics with Power Conversion Efficiency Exceeding 20%. *Adv. Mater.* **2024**, *36*, No. 2400342.

(5) Zhu, L.; Zhang, M.; Zhou, G.; Wang, Z.; Zhong, W.; Zhuang, J.; Zhou, Z.; Gao, X.; Kan, L.; Hao, B.; et al. Achieving 20.8% organic solar cells via additive-assisted layer-by-layer fabrication with bulk p-i-n structure and improved optical management. *Joule* **2024**, *8*, 3153−3168.

(6) Mou, H.; Yin, Y.; Chen, H.; Xu, J.; Ding, J.; Ju, C.; Zhu, J.; Wang, Y.; Chen, W.; Xu, G.; et al. Transient Dipole Strategy Boosts Highly Oriented Self-Assembled Monolayers for Organic Solar Cells Approaching 21% Efficiency. *J. Am. Chem. Soc.* **2025**, *147*, 21241−21251.

(7) Xie, J.; Zhang, K.; Hao, L.; Yang, Z.; Dong, S.; Li, H.; Liu, L.; Yu, J.; Wang, L.; Zhao, J.; et al. Non-Halogenated Solvent-Processed Organic Solar Cells with Efficiencies Exceeding 20.0% and 110 cm^2 Modules Exceeding 13% Enabled by Film-Forming Dynamics Engineering. *Adv. Energy Mater.* **2025**, *15*, No. 2501819.

(8) Duan, X.; Song, J.; Zhang, J.; Zhuang, J.; Deng, J.; Wang, X.; Dai, G.; Song, B.; Qiao, J.; Hao, X.; et al. Green Solvent-Processed Organic Solar Cells Approaching 20.4% Efficiency via Active Layer Pre-Solidification. *Adv. Mater.* **2025**, *37*, No. 2503510.

(9) Li, K.; Xie, Q.; An, C.; Zhong, J.; Yao, Y.; Hong, C.; Chen, Y.; Geng, H.; Wu, Y.; Zhang, W.; et al. A Nonfused Ring Electron Acceptor with Aggregation-Induced Emission Assistance Achieving Over 20% Efficiency in Organic Solar Cells. *Angew. Chem., Int. Ed.* **2025**, *64*, No. e202506415.

(10) Chen, L.; Liang, W.; Sergeev, A.; Lai, J. Y. L.; Zeng, X.; Wong, K. S.; Zhang, J.; Pun, S. H.; Yan, H.; Hu, H. Benzannulation of furan: a strategy for stable and high-performance furan-containing giant electron acceptor with efficiency exceeding 20%. *Energy Environ. Sci.* **2025**, *18*, 6608−6617.

(11) Sun, F.; Wu, J.; Cheng, B.; Kan, L.; Hua, F.; Sun, W.; Wang, H.; Huo, Y.; Chen, S.; Xia, X.; et al. Constructing continuous acceptor fibrillar networks and achieving uniform phase separation via polymer-assisted morphology control for 20.3% efficiency additive-free organic solar cells. *Energy Environ. Sci.* **2025**, *18*, 7071−7081.

(12) Moulebhar, S.; Bendenia, C.; Bendenia, S.; Merad-Dib, H.; Khantar, S. A.; Merabet, S. High-efficiency design and optimization of 2 T monolithic polymer/polymer tandem solar cells using SCAPS-1D simulations. *Phys. Scr.* **2025**, *100*, No. 045108.

(13) Brédas, J.-L.; Norton, J. E.; Cornil, J.; Coropceanu, V. Molecular Understanding of Organic Solar Cells: The Challenges. *Acc. Chem. Res.* **2009**, *42*, 1691−1699.

(14) Mazzio, K. A.; Luscombe, C. K. The future of organic photovoltaics. *Chem. Soc. Rev.* **2015**, *44*, 78−90.

(15) Qian, D.; Zheng, Z.; Yao, H.; Tress, W.; Hopper, T. R.; Chen, S.; Li, S.; Liu, J.; Chen, S.; Zhang, J.; et al. Design rules for minimizing voltage losses in high-efficiency organic solar cells. *Nat. Mater.* **2018**, *17*, 703−709.

(16) Liu, J.; Duan, X.; Zhang, J.; Ge, Z.; Liu, L.; Qiao, J.; Li, Y.; Bi, Z.; Zhang, H.; Gao, J.; et al. Acridine-Substituted-Centronucleus Nonfullerene Acceptors Enables Organic Solar Cells with Over 20% Efficiency with Low Nonradiative Recombination Loss. *Angew. Chem., Int. Ed.* **2025**, *64*, No. e202500129.

(17) Lu, H.; Liu, W.; Jin, H.; Huang, H.; Tang, Z.; Bo, Z. High-Efficiency Organic Solar Cells with Reduced Nonradiative Voltage Loss Enabled by a Highly Emissive Narrow Bandgap Fused Ring Acceptor. *Adv. Funct. Mater.* **2022**, *32*, No. 2107756.

(18) Li, C.; Zhou, J.; Song, J.; Xu, J.; Zhang, H.; Zhang, X.; Guo, J.; Zhu, L.; Wei, D.; Han, G.; et al. Non-fullerene acceptors with branched side chains and improved molecular packing to exceed 18% efficiency in organic solar cells. *Nat. Energy* **2021**, *6*, 605−613.

(19) Bronstein, H.; Nielsen, C. B.; Schroeder, B. C.; McCulloch, I. The role of chemical design in the performance of organic semiconductors. *Nat. Rev. Chem.* **2020**, *4*, 66−77.

(20) Chen, J.; Zhang, W.; Wang, L.; Yu, G. Recent Research Progress of Organic Small-Molecule Semiconductors with High Electron Mobilities. *Adv. Mater.* **2023**, *35*, No. 2210772.

(21) Jiang, H.; Zhu, S.; Cui, Z.; Li, Z.; Liang, Y.; Zhu, J.; Hu, P.; Zhang, H.-L.; Hu, W. High-performance five-ring-fused organic semiconductors for field-effect transistors. *Chem. Soc. Rev.* **2022**, *51*, 3071−3122.

(22) Xie, Z.; Liu, D.; Gao, C.; Zhang, X.; Dong, H.; Hu, W. High Mobility Emissive Organic Semiconductors for Optoelectronic Devices. *J. Am. Chem. Soc.* **2025**, *147*, 2239−2256.
(23) Wang, W.; W, J.; Zhong, Z.; Jianhui, H. Research Progress of Tandem Organic Solar Cells. *Acta Chim. Sin.* **2020**, *78*, 382−396.
(24) Meng, L.; Zhang, Y.; Wan, X.; Li, C.; Zhang, X.; Wang, Y.; Ke, X.; Xiao, Z.; Ding, L.; Xia, R.; et al. Organic and solution-processed tandem solar cells with 17.3% efficiency. *Science* **2018**, *361*, 1094−1098.
(25) Im, Y.; Byun, S. Y.; Kim, J. H.; Lee, D. R.; Oh, C. S.; Yook, K. S.; Lee, J. Y. Recent Progress in High-Efficiency Blue-Light-Emitting Materials for Organic Light-Emitting Diodes. *Adv. Funct. Mater.* **2017**, *27*, No. 1603007.
(26) Kang, J.; Shin, D. J.; Lee, J. Y. Recent Advances in Narrow Emission Bandwidth Materials for Application in Organic Light-Emitting Diodes. *Adv. Opt. Mater.* **2025**, *13*, No. 2402653.
(27) Liu, Y.; Li, C.; Ren, Z.; Yan, S.; Bryce, M. R. All-organic thermally activated delayed fluorescence materials for organic light-emitting diodes. *Nat. Rev. Mater.* **2018**, *3*, No. 18020.
(28) Hatakeyama, T.; Shiren, K.; Nakajima, K.; Nomura, S.; Nakatsuka, S.; Kinoshita, K.; Ni, J.; Ono, Y.; Ikuta, T. Ultrapure Blue Thermally Activated Delayed Fluorescence Molecules: Efficient HOMO−LUMO Separation by the Multiple Resonance Effect. *Adv. Mater.* **2016**, *28*, 2777−2781.
(29) Liu, X.; Pang, S.; Zeng, L.; Deng, W.; Yang, M.; Yuan, X.; Li, J.; Duan, C.; Huang, F.; Cao, Y. An electron acceptor featuring a B−N covalent bond and small singlet−triplet gap for organic solar cells. *Chem. Commun.* **2022**, *58*, 8686−8689.
(30) Li, G.; Xu, K.; Zheng, J.; Fang, X.; Yang, Y.-F.; Lou, W.; Chu, Q.; Dai, J.; Chen, Q.; Yang, Y.; She, Y. B. Double boron−oxygen-fused polycyclic aromatic hydrocarbons: skeletal editing and applications as organic optoelectronic materials. *Nat. Commun.* **2023**, *14*, No. 7089.
(31) Li, G.; Xu, K.; Zheng, J.; Fang, X.; Lou, W.; Zhan, F.; Deng, C.; Yang, Y.-F.; Zhang, Q.; She, Y. High-Performance Ultraviolet Organic Light-Emitting Diodes Enabled by Double Boron−Oxygen-Embedded Benzo[m]tetraphene Emitters. *J. Am. Chem. Soc.* **2024**, *146*, 1667−1680.
(32) Yuan, J.; Zhang, Y.; Zhou, L.; Zhang, G.; Yip, H.-L.; Lau, T.-K.; Lu, X.; Zhu, C.; Peng, H.; Johnson, P. A.; et al. Single-Junction Organic Solar Cell with over 15% Efficiency Using Fused-Ring Acceptor with Electron-Deficient Core. *Joule* **2019**, *3*, 1140−1151.
(33) Lin, Y.; Wang, J.; Zhang, Z.-G.; Bai, H.; Li, Y.; Zhu, D.; Zhan, X. An Electron Acceptor Challenging Fullerenes for Efficient Polymer Solar Cells. *Adv. Mater.* **2015**, *27*, 1170−1174.
(34) Lu, T.; Chen, F. Multiwfn: A multifunctional wavefunction analyzer. *J. Comput. Chem.* **2012**, *33*, 580−592.
(35) Lu, T. A comprehensive electron wavefunction analysis toolbox for chemists, Multiwfn. *J. Chem. Phys.* **2024**, *161*, No. 082503, DOI: 10.1063/5.0216272.
(36) Wan, X.; Li, C.; Zhang, M.; Chen, Y. Acceptor−donor−acceptor type molecules for high performance organic photovoltaics − chemistry and mechanism. *Chem. Soc. Rev.* **2020**, *49*, 2828−2842.
(37) Ji, X.; Wang, T.; Fu, Q.; Liu, D.; Wu, Z.; Zhang, M.; Woo, H. Y.; Liu, Y. Deciphering the Effects of Molecular Dipole Moments on the Photovoltaic Performance of Organic Solar Cells. *Macromol. Rapid Commun.* **2023**, *44*, No. 2300213.
(38) Li, Z.; Zhang, W.; Xu, X.; Genene, Z.; Di Carlo Rasi, D.; Mammo, W.; Yartsev, A.; Andersson, M. R.; Janssen, R. A. J.; Wang, E. High-Performance and Stable All-Polymer Solar Cells Using Donor and Acceptor Polymers with Complementary Absorption. *Adv. Energy Mater.* **2017**, *7*, No. 1602722.
(39) Zhang, M.; Guo, X.; Ma, W.; Ade, H.; Hou, J. A Large-Bandgap Conjugated Polymer for Versatile Photovoltaic Applications with High Performance. *Adv. Mater.* **2015**, *27*, 4655−4660.
(40) Park, I. S.; Matsuo, K.; Aizawa, N.; Yasuda, T. High-Performance Dibenzoheteraborin-Based Thermally Activated Delayed Fluorescence Emitters: Molecular Architectonics for Concurrently Achieving Narrowband Emission and Efficient Triplet−Singlet Spin Conversion. *Adv. Funct. Mater.* **2018**, *28*, No. 1802031.
(41) Santoro, F.; Lami, A.; Improta, R.; Bloino, J.; Barone, V. Effective method for the computation of optical spectra of large molecules at finite temperature including the Duschinsky and Herzberg−Teller effect: The Qx band of porphyrin as a case study. *J. Chem. Phys.* **2008**, *128*, No. 224311, DOI: 10.1063/1.2929846.
(42) Shi, Y.; Chang, Y.; Lu, K.; Chen, Z.; Zhang, J.; Yan, Y.; Qiu, D.; Liu, Y.; Adil, M.; Ma, W.; Hao, X.; Zhu, L.; Wei, Z. Small reorganization energy acceptors enable low energy losses in non-fullerene organic solar cells. *Nat. Commun.* **2022**, *13*, No. 3256.
(43) Zhao, L.; Li, J.; Li, L.; Hu, W. Recent advances in small-molecule organic fluorescent semiconductors. *J. Mater. Chem. C* **2024**, *12*, 13745−13761.
(44) Ma, S.; Du, S.; Pan, G.; Dai, S.; Xu, B.; Tian, W. Organic molecular aggregates: From aggregation structure to emission property. *Aggregate* **2021**, *2*, No. e96.
(45) Hartnagel, P.; Kirchartz, T. Understanding the Light-Intensity Dependence of the Short-Circuit Current of Organic Solar Cells. *Adv. Theor. Simul.* **2020**, *3*, No. 2000116.
(46) Würfel, U.; Perdigón-Toro, L.; Kurpiers, J.; Wolff, C. M.; Caprioglio, P.; Rech, J. J.; Zhu, J.; Zhan, X.; You, W.; Shoaee, S.; et al. Recombination between Photogenerated and Electrode-Induced Charges Dominates the Fill Factor Losses in Optimized Organic Solar Cells. *J. Phys. Chem. Lett.* **2019**, *10*, 3473−3480.